bioRxiv preprint doi: https://doi.org/10.1101/2020.10.18.344598; this version posted October 19, 2020. The copyright holder for this preprint (which was not certified by peer review) is the author/funder, who has granted bioRxiv a license to display the preprint in perpetuity. It is made available under aCC-BY-NC-ND 4.0 International license.

PIEZO1-induced cellular retraction controls keratinocyte migration in wound healing

Jesse R. Holt* [1,2,3], Wei-Zheng Zeng* [4], Elizabeth L. Evans* [1,2], Seung-Hyun Woo* [4], Shang Ma [4], Hamid Abuwarda [1,2], Meaghan Loud [4], Ardem Patapoutian [4†], Medha M. Pathak [1,2,3,5†]

[1] Department of Physiology & Biophysics, UC Irvine, Irvine, CA, 92697, USA

[2] Sue and Bill Gross Stem Cell Research Center, UC Irvine, Irvine, CA, 92697, USA

[3] Center for Complex Biological Systems, UC Irvine, Irvine, CA, 92697, USA

[4] Howard Hughes Medical Institute, Department of Neuroscience, The Scripps Research Institute, La Jolla, CA 92037, USA

[5] Department of Biomedical Engineering, UC Irvine, Irvine, CA, 92697, USA

* Equal contribution

[†] Corresponding authors (ardem@scripps.edu; medhap@uci.edu)

Abstract

Keratinocytes are the predominant cell type of the epidermis and form an important protective barrier to the external environment. During the healing of wounded skin, keratinocytes migrate from the wound edge to reinstate the epithelial barrier [1,2]. Mechanical cues are important regulators of cell migration in this process [3–7]; however, the molecular transducers and biophysical mechanisms of this mechanoregulation remain elusive. Here, we show through molecular, cellular and organismal studies that the mechanically-activated ion channel PIEZO1 regulates keratinocyte migration through dynamic cellular localization which dictates retraction events. Single keratinocytes isolated from an epidermal-specific *Piezo1* knockout mouse moved faster and migrated farther than littermate controls. To determine how PIEZO1 may contribute to cell migration, we imaged the localization of endogenous channels in migrating keratinocytes over several hours. We found that enrichment of PIEZO1 channel puncta correlated with cellular retraction in migrating single cells and in collectively migrating monolayers. Strikingly, PIEZO1 activation with Yoda1 resulted in increased retraction events in single cells as well as in monolayers of keratinocytes. During *in vitro* scratch assays, Yoda1-induced activation of PIEZO1 caused slower wound closure due to increased retraction events at the wound. Conversely, channel deletion resulted in faster scratch wound closure. This result was mirrored *in vivo* whereby epidermal-specific PIEZO1 knockout mice exhibited faster wound closure compared to littermate controls, and epidermal-specific PIEZO1 gain-of-function mice displayed slower wound closure. Overall, our findings show that reducing Piezo1 activity can accelerate wound healing, suggesting a potential pharmacological target for wound treatment. More broadly, we show that molecular-scale spatiotemporal dynamics of Piezo1 channels controls tissue-scale cell migration, a cellular process of fundamental importance in development, homeostasis and repair.

Introduction

Cell migration is a fundamental cellular function that drives several physiological processes in development and tissue repair. During the repair of wounded skin, the migration of keratinocytes from the wound edge into the wound bed plays an essential step in reestablishing the epithelial barrier and restoring its protective functions [1,2]. A delay in wound closure puts the body at an increased risk of infection, disease and scar formation [5]. Accumulating evidence has

bioRxiv preprint doi: https://doi.org/10.1101/2020.10.18.344598; this version posted October 19, 2020. The copyright holder for this preprint (which was not certified by peer review) is the author/funder, who has granted bioRxiv a license to display the preprint in perpetuity. It is made available under aCC-BY-NC-ND 4.0 International license.

shown that mechanical cues and cell-generated traction forces play an important role in regulating the healing process and wound closure [5–9]. However, the molecular identity of keratinocyte mechanotransducers that control cellular locomotion remain unknown.

Cells are able to sense and detect mechanical forces, converting them into biochemical signals through the process of mechanotransduction. One class of mechanosensors utilized by the cell are mechanically activated ion channels which offer the unique ability for cells to rapidly detect and transduce mechanical forces into electrochemical signals [10,11]. The Piezo1 ion channel has been shown to play an important role in a variety of cell types, and it regulates several key biological processes including vascular and lymphatic development, red blood cell volume regulation, stem cell fate, the baroreceptor response, cardiovascular homeostasis, cartilage mechanics, and others [12–19]. Previous studies in MDCK cells and in zebrafish larvae have demonstrated the importance of the channel in the homeostatic regulation of epithelial cell numbers [20,21]. As yet, the role of Piezo1 in skin wound healing, an important epithelial function, has not been investigated. We recently showed that Piezo1 acts as a key transducer of nonmuscle myosin-II mediated cellular traction forces [14,22]. Since mechanical force generation by myosin-II is critically important in cell migration [4,23,24], we asked whether Piezo1 may function as a mechanosensor regulating cell migration and keratinocyte reepithelialization during the wound healing process. Here we show that Piezo1 activity reduces efficiency of keratinocyte migration and wound healing. It achieves this via dynamic sub-cellular localization, concentrating at areas of the wound edge and causing local retraction at these regions.

Results

PIEZO1 activity regulates keratinocyte migration

Analysis of *Piezo* channel mRNA expression in mouse tissues has previously shown that *Piezo1* is highly expressed in skin, while *Piezo2* is less abundant [25]. To characterize PIEZO1 expression in skin, we used a reporter mouse expressing a promoter-less β-geo (β-gal and neomycin phosphotransferase) in-frame with a portion of the PIEZO1 channel [13]. LacZ staining of skin tissue from these reporter mice revealed a high expression of PIEZO1 in the epidermal layer of keratinocytes as well as in hair follicles (Fig. 1A).

Since the global knockout of *Piezo1* is embryonically lethal [12,13], we generated an epidermal-specific knockout mouse to investigate whether PIEZO1 plays a role in keratinocyte migration. The *Krt14Cre* mouse line was crossed with *Piezo1*$^{fl/fl}$ mice [18] to generate *Krt14Cre;Piezo1*$^{fl/fl}$ mice (hereafter referred to as conditional knockout, cKO) which are viable and develop normally (Supplementary Fig. 1), consistent with observations by Moehring et al [26]. qRT-PCR analysis using keratinocytes from *Piezo1* cKO and control animals confirmed the expression of *Piezo1* but not of *Piezo2* in control mice (Supplementary Fig. 2), and showed that *Piezo1* mRNA expression is efficiently abrogated in cells from littermate cKO animals (Fig. 1B). Furthermore, we also generated the line of *Krt14Cre;Piezo1*$^{cx/+}$ mouse line which expresses the gain of function (GoF) *Piezo1* mutation, R2482H [27], in keratinocytes.

We previously reported that in adherent cells Piezo1 produces Ca^{2+} flickers in response to cell-generated forces in the absence of external mechanical stimulation [14,22]. In order to assess functional PIEZO1 activity in keratinocytes, we performed Ca^{2+} imaging using Total Internal Reflection Fluorescence Microscopy (TIRFM) of keratinocytes isolated from *Piezo1* cKO, GoF,

bioRxiv preprint doi: https://doi.org/10.1101/2020.10.18.344598; this version posted October 19, 2020. The copyright holder for this preprint (which was not certified by peer review) is the author/funder, who has granted bioRxiv a license to display the preprint in perpetuity. It is made available under aCC-BY-NC-ND 4.0 International license.

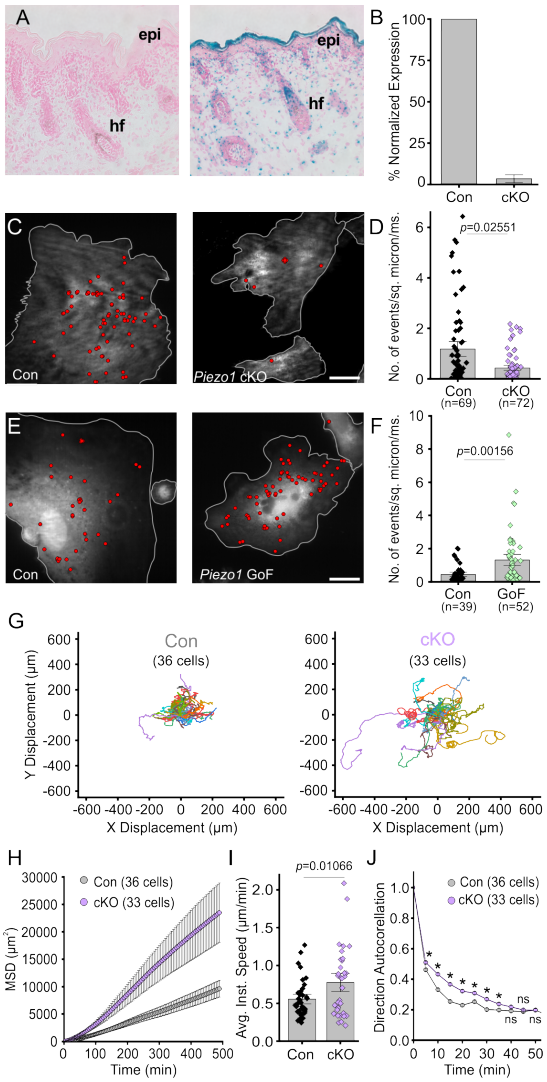

Figure 1. PIEZO1 is expressed in keratinocytes, produces Ca^{2+} flickers and regulates cell migration speed. **(A)** Representative images of LacZ stained Piezo1$^{+/+}$ (*left*) and Piezo$^{+/\beta Geo}$ (*right*) skin sections from P2 (postnatal day 2) mice. epi, epidermis. hf, hair follicle. **(B)** qRT-PCR from primary neonatal keratinocytes of Piezo1 mRNA expression in Krt14$^{+/+}$ *Piezo1$^{fl/fl}$* (Con) and *Krt14$^{Cre/+}$;Piezo1$^{fl/fl}$* (cKO) mice. See also Supplementary Figures 1-2. Data collected from 2 litters. **(C)** Representative images of sites of Ca^{2+} flickers (red dots) overlaid on images of keratinocytes isolated from control (*left*) and littermate *Piezo1*-cKO (*right*) mice that are loaded with fluorescent Ca^{2+} indicator Cal-520AM. Grey line denotes cell boundary, Scale Bar = 20 μm. **(D)** Frequency of Ca^{2+} flickers in *Piezo1*-cKO and respective control cells. n in D denotes the number of videos (i.e., unique fields of view imaged, each of which is composed of one or more cells). Videos were collected from 4 independent experiments from 3 litters. See also Supplementary Video 1 and Supplementary Figure 3. **(E, F)** Similar to C, D but using keratinocytes from control (*left*) and littermate *Krt14Cre;Piezo1$^{cx/+}$* (GoF) (*right*) mice. Videos were collected from 4 independent experiments from 3 litters. See also Supplementary Video 2 and Supplementary Figure 3. **(G)** Cell trajectories derived from tracking individual migrating keratinocytes using Differential Interference Contrast (DIC) time lapse imaging. Keratinocytes were isolated from control (*left*) and respective *Piezo1*-cKO littermates (*right*). Trajectories are shown with cell position at time point 0 normalized to the origin. **(H)** Mean squared displacement (MSD) analysis of control and *Piezo1*-cKO keratinocytes tracked in G. Average MSD is plotted as a function of time. Error bars (S.E.M) are smaller than symbols at some points. **(I)** Quantitation of the average instantaneous speed from individual *Piezo1*-cKO keratinocytes relative to littermate control cells. **(J)** Average direction autocorrelation measurement of *Piezo1-cKO*and control keratinocytes plotted as a function of time interval. * denotes a statistically significant difference, and ns denotes "not statistically significant". From left to right: p= 2.0307x10^{-4}, 5.75675 x10^{-14}, 3.18447 x10^{-15}, 5.34662 x10^{-10}, 1.72352 x10^{-4}, 1.34648 x10^{-5}, 0.01951, 0.13381, 0.61758 as determined by Kruskal-Wallis test. Plotted error bars (S.E.M) are smaller than symbols. Data are from 3 independent experiments from 2 litters. See also Supplementary Video 3 and Supplementary Figure 4. All bars denote mean ± S.E.M.

bioRxiv preprint doi: https://doi.org/10.1101/2020.10.18.344598; this version posted October 19, 2020. The copyright holder for this preprint (which was not certified by peer review) is the author/funder, who has granted bioRxiv a license to display the preprint in perpetuity. It is made available under aCC-BY-NC-ND 4.0 International license.

and their respective control (Cre-) littermates loaded with a fluorescent calcium indicator, Cal-520 AM. Similar to our previous observations, we observed localized Ca^{2+} flickers in the absence of external mechanical stimulation (Fig. 1C, Supplementary Video 1). *Piezo1*-cKO keratinocytes showed reduced flicker activity compared to cells from littermate control mice (Fig. 1C, 1D, Supplementary Video 1, Supplementary Fig. 3A). Unlike fibroblasts, where *Piezo1* knockout resulted in over 90% reduction of Ca^{2+} flicker signals [22], *Piezo1*-cKO keratinocytes show a 63% reduction in mean Ca^{2+} flicker frequency, consistent with reports that keratinocytes also express other Ca^{2+}-permeable ion channels [28–30]. On the other hand, *Piezo1*-GoF cells displayed a 2.95-fold increase in flicker frequency relative to littermate controls, providing additional confirmation that keratinocytes express functional PIEZO1 channels (Fig. 1E, 1F, Supplementary Video 2, Supplementary Fig. 3B). Some differences in the frequency of events between the control cKO and control GoF cells were observed, likely arising from the different genetic backgrounds of the two strains. Taken together, these results demonstrate that *Piezo1* expression contributes to Ca^{2+} flickers elicited by cell-generated forces in keratinocytes.

Cell-generated forces orchestrate several sub-cellular processes during cell migration [23,31]; hence we asked whether the cell-generated PIEZO1 activity observed above may be involved in cell migration. We captured the migration dynamics of dissociated single keratinocytes from *Piezo1*-cKO mice. Isolated cells were sparsely seeded onto fibronectin-coated glass-bottom dishes and imaged over several hours using differential interference contrast (DIC) time-lapse imaging. We tracked the position of individual cells in the acquired movies and analyzed the extracted cell migration trajectories using an open-source algorithm, DiPer [32]. The time-lapse images (Supplementary Video 3), and corresponding cell migration trajectories (Fig. 1G; Supplementary Fig. 4) revealed that the migration patterns of *Piezo1*-cKO keratinocytes are distinct from their littermate control cells. To quantify cellular migration, we generated mean squared displacement (MSD) plots which provide a measure of the surface area explored by the cells, i.e. of the overall efficiency of migration. Interestingly, *Piezo1*-cKO keratinocytes explored a larger area compared to littermate control cells (Fig. 1H).

The MSD of a migrating cell is determined by two parameters: displacement rate (speed) and directional persistence (propensity of the cell to move in a straight line). The average instantaneous speed calculated by DiPer analysis was higher for *Piezo1*-cKO cells relative to littermate control cells (Fig. 1I). To assess directional persistence, we performed direction autocorrelation analysis, a robust measure of migration directionality that, unlike the more commonly used directional ratio analysis, is not confounded by differences in migration speed [32]. The direction autocorrelation function for trajectories from *Piezo1*-cKO keratinocytes decayed slower than for littermate control cells, indicative of fewer turns (Fig. 1J). Thus, *Piezo1*-cKO keratinocytes migrate faster and straighter. Overall, our data demonstrate that PIEZO1 regulates keratinocyte migration, with channel activity resulting in less efficient cellular migration.

Piezo1 activation causes cellular retraction

To understand how PIEZO1 regulates keratinocyte motility, we visualized its localization in keratinocytes harvested from a *Piezo1*-tdTomato fusion knock-in reporter mouse [13]. Using this model, we previously reported punctate membrane localization of endogenous PIEZO1-tdTomato channels in neural stem/progenitor cells and mouse embryonic fibroblasts in fixed and live cells by immunostaining and live-cell TIRF microscopy, respectively [22]. Here,

bioRxiv preprint doi: https://doi.org/10.1101/2020.10.18.344598; this version posted October 19, 2020. The copyright holder for this preprint (which was not certified by peer review) is the author/funder, who has granted bioRxiv a license to display the preprint in perpetuity. It is made available under aCC-BY-NC-ND 4.0 International license.

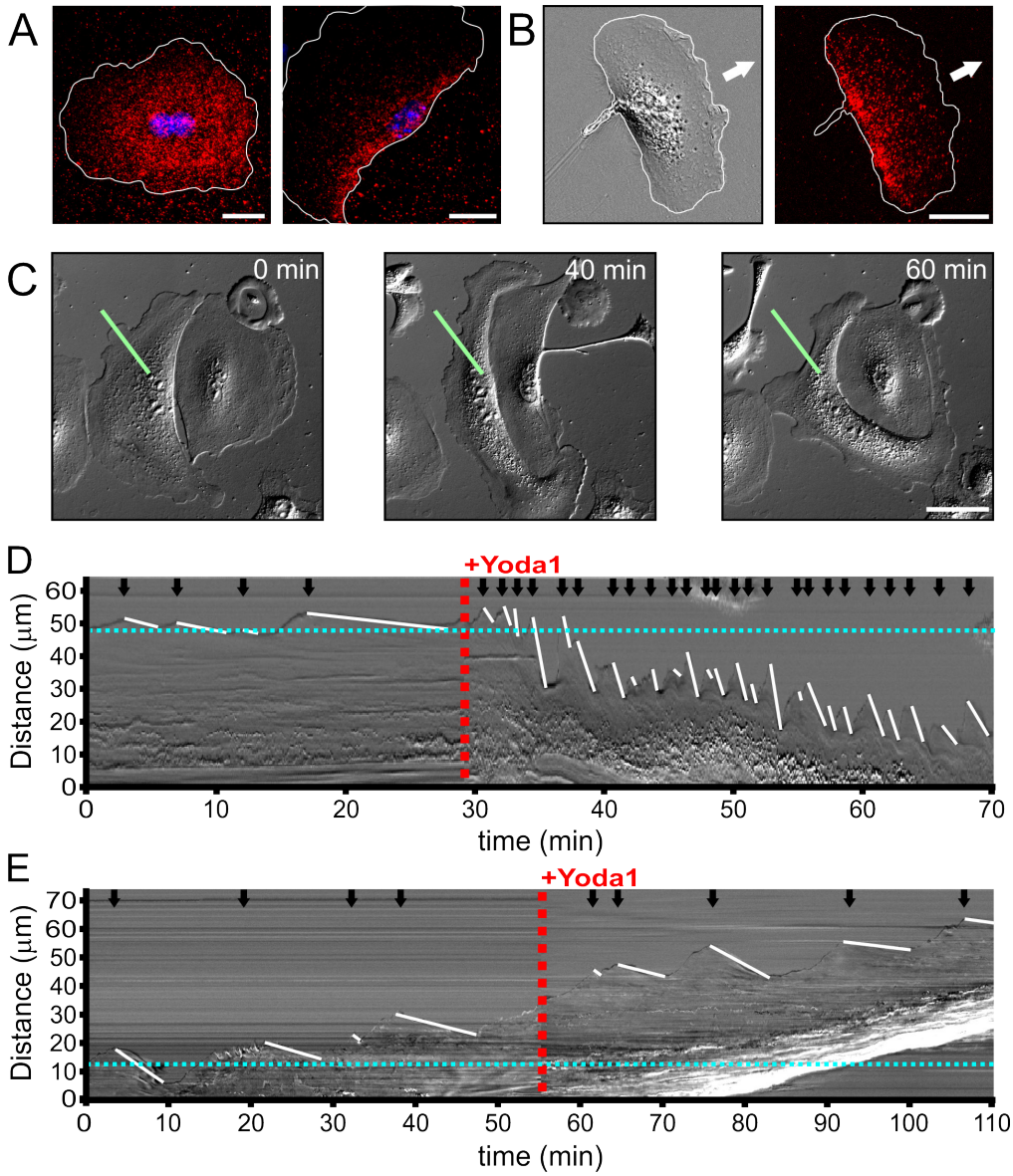

Figure 2. PIEZO1 activity promotes cellular retraction. (A) Representative TIRFM images of a non-polarized keratinocyte (*left*) and polarized keratinocyte (right) immuno-labeled with an antibody against RFP (red) and nuclear stain Hoechst (blue). White lines denote the cell boundary. Scale Bar = 20 μm. **(B)** Representative DIC (*left*) and TIRF (*right)* images illustrating the location of PIEZO1-tdTomato protein in live migrating keratinocytes. White lines denote the cell boundary. Scale Bar = 20 μm. See also Supplementary Video 4. **(C)** Images from a DIC time-lapse series of keratinocytes at time 0, 40 and 60 minutes. 4 μM Yoda1 was added to the bath solution after 30 minutes of baseline recording. The green lines denote the region of interest used for generating the kymograph in panel D. Scale Bar = 50 μm. **(D)** DIC kymograph of the keratinocyte presented in C. The red dotted line denotes the addition of 4 μM Yoda1. The black arrows indicate retraction events and the slope of the descending white lines denotes the velocity of retraction. Dotted blue line denotes starting position of the cell edge. See also Supplementary Video 5. **(E)** DIC kymograph of a *Piezo1*-cKO keratinocyte with the same annotations as D. See also Supplementary Video 6 and 7.

we similarly examined PIEZO1 localization, first in fixed keratinocytes by immunostaining for tdTomato. In non-polarized keratinocytes without an obvious migratory morphology, we observed PIEZO1-tdTomato puncta distributed throughout the cell (Fig. 2A, left). However, in keratinocytes that displayed an overt lamellipodium, a highly dynamic sheet-like organelle at the leading edge of migrating cells [33], PIEZO1-tdTomato localization often displayed a gradi-

bioRxiv preprint doi: https://doi.org/10.1101/2020.10.18.344598; this version posted October 19, 2020. The copyright holder for this preprint (which was not certified by peer review) is the author/funder, who has granted bioRxiv a license to display the preprint in perpetuity. It is made available under aCC-BY-NC-ND 4.0 International license.

ent, with higher PIEZO1 levels at the trailing or rear end of the cell (Fig. 2A, right). To confirm this observation, we directly imaged endogenous PIEZO1-tdTomato's subcellular localization in live, migrating keratinocytes using TIRFM imaging. By tracking the cells over time we confirmed that enrichment of PIEZO1-tdTomato puncta occurred at the rear end of the cell (Fig. 2B, Supplementary Video 4). The rear end of a migrating cell is an important determinant of its migratory behavior: nonmuscle myosin II-mediated contractile forces in this region induce and maintain polarization of the cell along the direction of migration and are responsible for the retraction of the rear end [34,35]. Since myosin II activation is enhanced by intracellular Ca^{2+} [36], we reasoned that higher PIEZO1 levels at the trailing end of the cell may suggest that its activity is involved in the generation of contractile forces during retraction.

Myosin II-mediated retraction is important not only at the rear end but also at the leading edge of the cell: cell migration progresses by iterative cycles of protrusion and retraction at the lamellipodia, where a myosin II-mediated retraction event sets the stage for the next protrusion event [37–39]. We reasoned that if PIEZO1 activity promotes contractile forces responsible for retraction, then increasing PIEZO1 activity by treatment of the Piezo1-agonist Yoda1 should also increase lamellipodial retraction events. Using DIC imaging of migrating keratinocytes, we monitored lamellipodial dynamics under control conditions and following Yoda1 treatment (Fig. 2C, Supplementary Video 5). To analyze lamellipodial dynamics over time we utilized kymographs to graphically represent movement of the keratinocyte leading edge over time (Fig. 2D). As expected, we observed that the cell edge undergoes cycles of protrusion and retraction. PIEZO1 activation by 4 μM Yoda1 resulted in an extremely dynamic cell edge (Fig. 2D, Supplementary Video 5). The frequency as well as the velocity of lamellipodial retractions increased upon PIEZO1 activation and resulted in a net cellular retraction over time (Fig. 2D, Supplementary Video 5); some cells demonstrated drastic retraction with Yoda1 treatment (Supplementary Video 6). *Piezo1*-cKO keratinocytes treated with 4 μM Yoda1 did not show an increase in retraction upon treatment with Yoda1 (Fig. 2E, Supplementary Video 7), demonstrating that increased retraction is mediated by PIEZO1.

Dynamic PIEZO1 localization informs retraction events during wound healing

We then asked whether PIEZO1-mediated retraction events observed in single cells are relevant in the context of a wounded cell monolayer, wherein cells migrate collectively to close the wound gap. We generated a scratch wound in a confluent monolayer of *Piezo1*-tdTomato keratinocytes and imaged spatiotemporal dynamics of PIEZO1-tdTomato localization at the cell-substrate interface using TIRFM imaging together with DIC imaging over the period of several hours. We found that immediately after scratch generation PIEZO1-tdTomato puncta showed no obvious enrichment (Supplementary Fig. 5), but this changed over the course of a few hours: by approximately 6 hours after wound generation PIEZO1 was enriched in band-like structures at non-contiguous regions of the wound edge (Fig. 3A, Fig. 3B). Interestingly, this enrichment was highly dynamic, such that channel enrichment ebbed and flowed over the course of the imaging period (Supplementary Videos 8 and 9).

Upon closer examination, we noticed retraction of the wound edge following enrichment of PIEZO1-tdTomato puncta. In some cases (as depicted in Figure 3B), channel enrichment was maintained for several hours and was accompanied by a sustained and overt retraction of the wound edge throughout that period (Fig. 3B, Supplementary Video 8). In other cases, PIEZO1

bioRxiv preprint doi: https://doi.org/10.1101/2020.10.18.344598; this version posted October 19, 2020. The copyright holder for this preprint (which was not certified by peer review) is the author/funder, who has granted bioRxiv a license to display the preprint in perpetuity. It is made available under aCC-BY-NC-ND 4.0 International license.

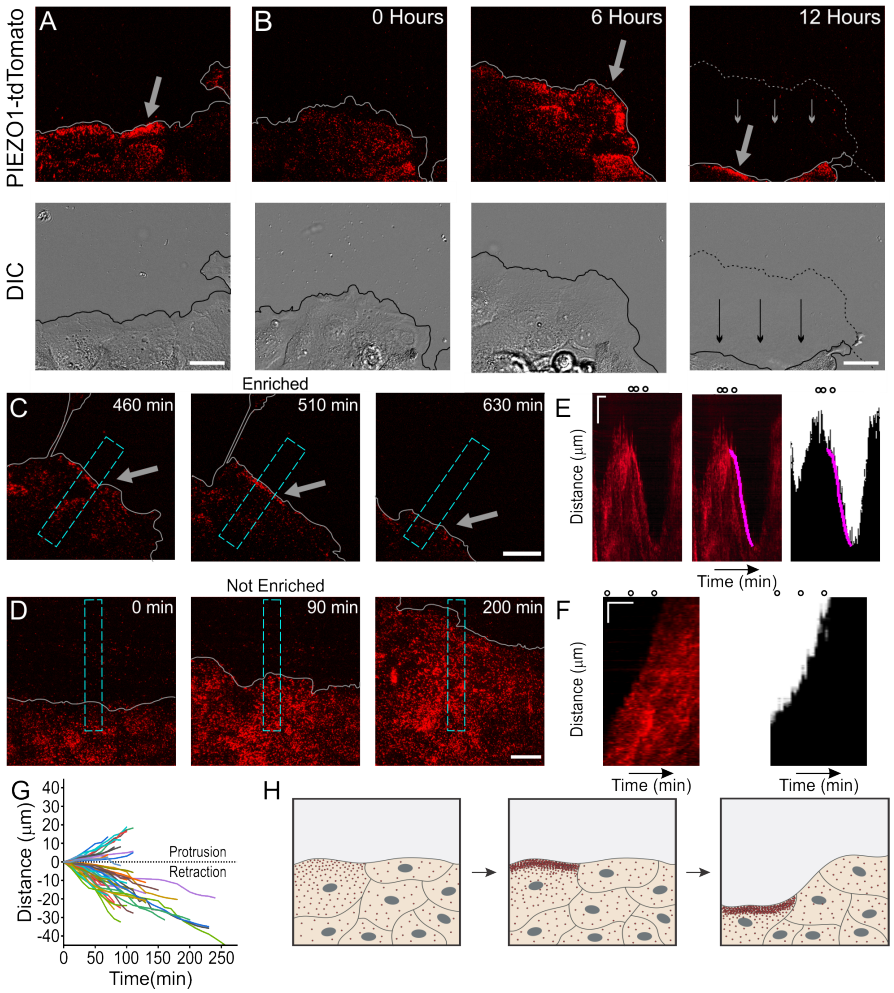

Figure 3. PIEZO1 channel enrichment is correlated with cell retraction in wound-healing monolayers. (A) Representative DIC (*bottom*) and TIRF (*top)* images visualizing the location of PIEZO1-tdTomato protein in live collectively migrating keratinocytes in an *in vitro* scratch assay. Grey (*top*) and black (*bottom*) lines denote the boundary of the cell monolayer. Grey arrow indicates region of PIEZO1 enrichment. Scale Bar = 20 µm. See also Supplementary Figure 5. **(B)** Representative DIC (*bottom*) and TIRF (*top*) images during a time-lapse imaging series following scratch generation at 0 hours showing PIEZO1-tdTomato localization and monolayer position. Grey (*top*) and black (*bottom*) lines denote the cell boundary. Dotted line in the 12-hour image denotes the position of the monolayer at 6 hours; small arrows indicate direction of monolayer movement during this period. Large grey arrow indicates region of PIEZO1 enrichment. Scale Bar = 20 µm. See also Supplementary Video 8. **(C, D)** Representative TIRF images taken from time-lapse image series of healing monolayers from PIEZO1-tdTomato keratinocytes highlighting fields of view in which PIEZO1-tdTomato is enriched **(C)** or not enriched **(D)** at the monolayer's leading edge. Grey lines denote the boundary of the cell monolayer. Arrow indicates regions of enrichment. Scale Bars = 20 µm. Blue dashed rectangles in C & D depict the regions used to generate kymographs in E and F. TIRF Images were acquired every 10 minutes over a period of 16.6 hours. **(E, F)** *Left panels*: Representative kymographs illustrating PIEZO1-tdTomato puncta dynamics during the time-lapse series shown in C and D, respectively. *Middle Panel (for E only):* Magenta line denotes periods of PIEZO1-tdTomato puncta enrichment at the wound edge, identified and tracked using the deep learning-based kymograph analysis software, Kymobutler. No Kymobutler tracks were detected in non-enriched regions *(F)*. *Right panels*: Representative kymographs from binarized image of DIC images corresponding to C and D respectively, with Kymobutler track output from the middle panel overlaid. The cell monolayer is represented in black, and white denotes cell-free space of the wounded area. Note the PIEZO1-tdTomato enrichment track correlates with period of cell retraction. Scale Bar = 10 µm. Time bar = 100 minutes. Black open circles on top represent the time-points of images shown in C and D. **(G)** Plot showing 54 individual PIEZO1-tdTomato Kymobutler tracks from 25 kymographs collected from 3 independent experiments after normalizing the starting spatial and time coordinates of each track to the origin. See also Supplementary Videos 9, and 10. **(H)** Schematic of a healing monolayer indicating distributed Piezo1 localization (red dots) immediately post scratch (*left*), the development of areas of Piezo1 enrichment (*middle*) and subsequent retraction of those areas (*right*).

bioRxiv preprint doi: https://doi.org/10.1101/2020.10.18.344598; this version posted October 19, 2020. The copyright holder for this preprint (which was not certified by peer review) is the author/funder, who has granted bioRxiv a license to display the preprint in perpetuity. It is made available under aCC-BY-NC-ND 4.0 International license.

enrichment and the accompanying retraction lasted for shorter periods of time (Fig. 3C and Supplementary Video 9), and the periods without channel enrichment were accompanied by wound edge protrusion. To systematically assess the correlation of PIEZO1-tdTomato enrichment with wound edge retraction, we used kymographs to graphically represent puncta position across the imaging period (Fig. 3E). PIEZO1-tdTomato enrichment events at the wound edge appeared as linear streaks in the kymographs (Fig. 3E, left panel). We then utilized Kymobutler, a deep-learning-based kymograph analysis software [40] for unbiased detection of PIEZO1-tdTomato enrichment events (Fig. 3E, middle and right panels). Interestingly, for the kymographs from fields of view which did not show any apparent PIEZO1-tdTomato puncta enrichment near the wound edge (Fig. 3D, Supplementary Video 10), Kymobutler analysis did not detect any tracks at the wound edge and we did not observe any retraction of the wound edge (Fig. 3F).

Kymobutler analysis of 25 kymographs displaying PIEZO-tdTomato enrichment yielded 54 PIEZO1-tdTomato tracks at the wound edge. 72% of these tracks exhibited a negative slope corresponding to cell edge retraction, while the other 28% of tracks displayed positive slopes (Fig. 3G). Taken together with the observations of PIEZO1-tdTomato dynamics in single cells, this analysis demonstrates that PIEZO1-tdTomato enrichment and activity correlates with cellular retraction. In wound-healing monolayers of keratinocytes, PIEZO1-tdTomato enrichment and retraction observed at the wound edge (Fig. 3H) suggests that PIEZO1 activity may increase cellular retraction and delay wound healing.

Reduced PIEZO1 accelerates wound healing

We next investigated the effect of PIEZO1 activity on keratinocyte re-epithelialization, a key event in skin wound healing. To mimic the *in vivo* wound healing paradigm, we generated scratch wounds in keratinocyte monolayers to trigger the re-epithelialization process, and allowed the monolayers to migrate toward each other. We performed DIC time-lapse imaging of the healing monolayer in the presence and absence of 4 μM Yoda1 to observe dynamics of the wound edge. In control conditions, the monolayer advanced forward (Fig. 4A, Supplementary Video 11), while in the presence of Yoda1 increased retraction events prevented the monolayer from advancing far into the wound bed (Fig. 4B, Supplementary Video 11). Furthermore, in scratch wound assays performed with Ibidi chambers (Fig. 4C), wound closure was significantly impaired when Yoda1 was added to healing control monolayers (Fig. 4D, left). Conversely, scratch wounds in monolayers of *Piezo1*-cKO keratinocytes closed faster than control cells (Fig. 4D, right), further strengthening the role of PIEZO1 in keratinocyte reepithelialization.

To investigate whether the PIEZO1-mediated effect on keratinocyte re-epithelialization is relevant *in vivo,* we generated full-thickness wounds on dorsal skin of *Piezo1* cKO, GoF and their respective control littermates and measured wound closure (Fig. 4E). Six days post wounding, *Piezo1*-GoF mice showed larger wound areas while *Piezo1*-cKO mice displayed significantly smaller wound areas relative to their control littermates (Fig. 4F). Collectively, our *in vitro* and *in vivo* data suggest that the PIEZO1 ion channel plays an important role in wound healing and Piezo1 channel activity contributes to slower wound re-epithelialization (Fig. 4G).

Discussion

Ca^{2+} signals control many aspects of cell migration, including lamellipodial dynamics, traction force generation, rear retraction, focal adhesion turnover and migration directionality

bioRxiv preprint doi: https://doi.org/10.1101/2020.10.18.344598; this version posted October 19, 2020. The copyright holder for this preprint (which was not certified by peer review) is the author/funder, who has granted bioRxiv a license to display the preprint in perpetuity. It is made available under aCC-BY-NC-ND 4.0 International license.

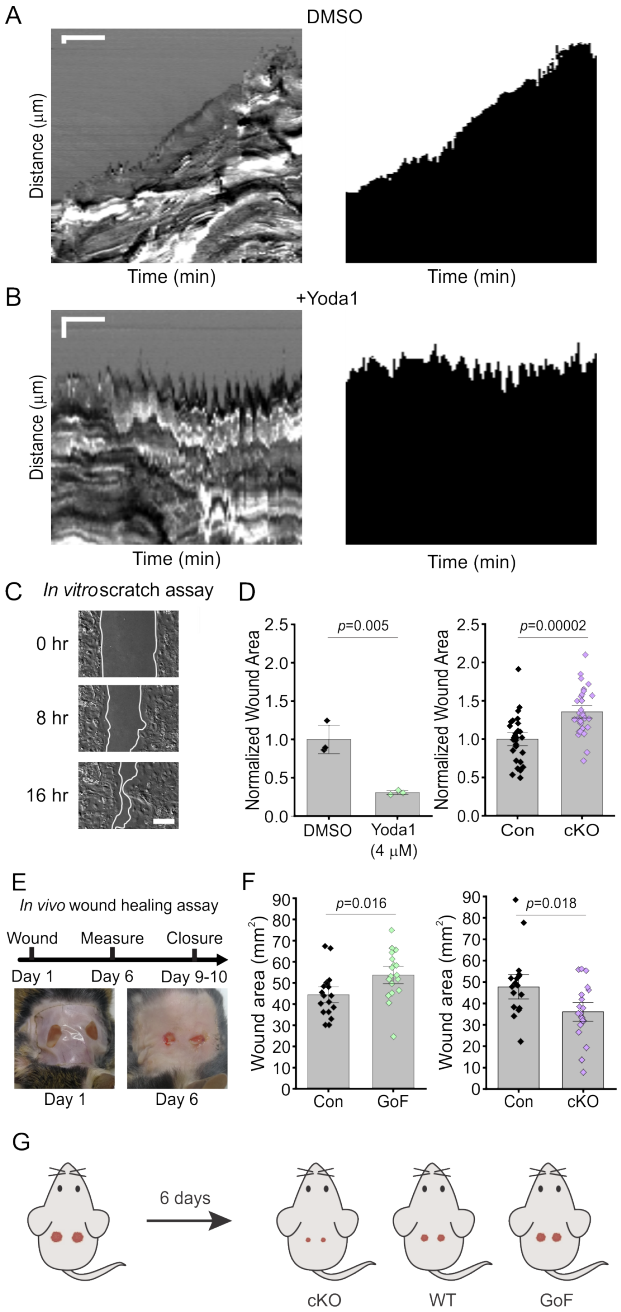

Figure 4. PIEZO1 activity slows wound healing. (A) Representative DIC kymograph taken at the wound edge, showing wound edge dynamics during an *in vitro* scratch assay in control (DMSO)-treated monolayers (*left*). Kymograph of binarized videos, with the cell monolayer represented in black and cell-free space of the wounded area in white (*right*). Scale Bar = 10 µm. Time bar = 100 min. See also Supplementary Video 11. **(B)** As for A but in a sample treated with 4 µM Yoda1. The data in A and B are representative of 3 independent experiments from keratinocytes from 3 litters. **(C)** Representative images of an *in vitro* scratch assay. White line represents the monolayer edge. Scale bar = 200 µm. **(D)** Quantification of scratch wound area (corresponding to area depicted between the two white lines in C, 16 hours after wound generation in DMSO-treated vs 4 µM Yoda1 treated cells (*left*; n = 3 independent experiments) or Control vs littermate *Piezo1*-cKO keratinocytes *(right)*; n = 29, WT, n = 31 *Piezo1*-cKO images from 3 independent experiments). Data are normalized to the control condition. **(E)** Diagram of *in vivo* wound healing model (*top*) and representative wound images at Day 0 and 6 (*bottom*). **(F)** Wound area of *Piezo1* GoF (*left*) and *Piezo1* cKO (*right*) groups at Day 6 relative to control (Con) littermates. Control (Con) refers to the Cre-negative littermates in each group (n = 18 wounds for Controls and *Piezo1* GoF, and n = 20 wounds for *Piezo1* cKO, with two wounds per animal). **(G)** Schematic illustrating results from *in vivo* wound healing assay shown in F. Mice were wounded (*left*) and after 6 days, wounds of *Piezo1*-cKO mice healed more than WT, whereas wounds from *Piezo1*-GoF mice healed less. All bars denote mean ± S.E.M.

bioRxiv preprint doi: https://doi.org/10.1101/2020.10.18.344598; this version posted October 19, 2020. The copyright holder for this preprint (which was not certified by peer review) is the author/funder, who has granted bioRxiv a license to display the preprint in perpetuity. It is made available under aCC-BY-NC-ND 4.0 International license.

[41–43]. While mechanically-activated ion channels were proposed to contribute to Ca^{2+} signaling in single cell migration *in vitro* as early as twenty years ago [44–48], many important questions have remained unanswered, including those related to channel identity, functional effects in collective cell migration and physiological contribution during wound healing. Here we identify a key mechanically-activated ion channel, PIEZO1, in controlling keratinocyte migration, and provide evidence for its involvement in cellular retraction events in single cells as well as in collective cell migration during wound healing. Piezo1 has previously been implicated in *in vitro* cell migration in different cell types, however the effect of channel modulation on migration has varied in the literature, likely due to a diversity of cell types and assays [49–53]. We show through a combination of orthogonal assays in single and collective migration studies that Piezo1 activity slows keratinocyte cell migration. Moreover, epidermal-specific *Piezo1* knockout resulted in faster healing in *in vivo* wound healing studies in mice, and conversely a *Piezo1* gain-of-function mutation slowed wound healing.

These findings provide physiological evidence for a mechanically-activated ion channel in wound healing and suggest potential therapeutics through a targeted inhibition of Piezo1, perhaps applied topically, that could help speed wound healing, potentially reducing risk of infection. Given that speedy wound healing affords an evolutionary advantage and that PIEZO1 activity slows wound healing, a puzzling question arises regarding the role of PIEZO1 expression in keratinocytes. Perhaps, the channel also performs other important functions in these cells. Consistent with this idea, a recent study by Moehring *et al.* reports that keratinocyte PIEZO1 is critical for sensory afferent firing and behavioral responses to innocuous and noxious mechanical stimulation [26].

One of the most surprising findings to emerge from our studies is the highly dynamic nature of the spatial localization and enrichment of PIEZO1 channels in keratinocytes. Based on this finding, we propose a novel mechanism regulating cell migration wherein spatiotemporal enrichment of PIEZO1 channels serves to localize and amplify channel activity, and the resulting contractile force, to control cellular retraction events. It is well established that retraction during cell migration occurs due to force generated by Myosin II [33,54], and we previously showed that Myosin II mediated cellular traction forces elicit localized Piezo1 Ca^{2+} flickers [22]. Taken together, these findings suggest that Piezo1 may induce cellular retraction through a feedforward loop between Piezo1 and Myosin II as follows: traction force generation by Myosin II causes Piezo1-mediated Ca^{2+} influx, which in turn may increase Myosin II phosphorylation and force generation through the Ca^{2+}-regulated Myosin Light Chain Kinase. Enrichment of Piezo1 in subcellular regions would amplify this effect and result in a localized retraction.

Cell migration involves a complex orchestration of sub-cellular dynamics in which cytoskeletal events in different compartments of the cell need to be implemented in a precise spatiotemporal order. How this is achieved remains an open question. Our findings suggest that spatiotemporal enrichment dynamics of Piezo1 may play a role in this coordination. More broadly, our findings provide a mechanism by which nanoscale dynamics of Piezo1 channels can control tissue-scale cell migration, a finding with implications beyond wound healing to processes as diverse as development, homeostasis, disease and repair.

bioRxiv preprint doi: https://doi.org/10.1101/2020.10.18.344598; this version posted October 19, 2020. The copyright holder for this preprint (which was not certified by peer review) is the author/funder, who has granted bioRxiv a license to display the preprint in perpetuity. It is made available under aCC-BY-NC-ND 4.0 International license.

Acknowledgements

We thank Jamison Nourse and Gabriella Bertaccini for technical support, Vivian Leung for help with illustrations, and members of the lab for comments on the manuscript. This work was supported by NIH grants DP2AT010376 and R01NS109810 to M.M.P; NIH grant R01HL143297 to A.P., a James H. Gilliam Fellowship for Advanced Study (GT11549) from the Howard Hughes Medical Institute to M.M.P. and J.R.H., a postdoctoral fellowship from the George Hewitt Foundation for Medical Research to W.-Z.Z., and a seed grant to J.R.H and W.-Z.Z. from the UCI NSF-Simons Center for Multiscale Cell Fate Research (funded by NSF grant DMS1763272 and a Simons Foundation grant 594598). A.P. is an investigator of the Howard Hughes Medical Institute.

Author Contributions

Conceptualization, A.P. S-H.W, M.M.P; *Experimental design,* J.R.H., W-Z.Z., S-H.W, S.M., E.L.E, H.A., M.M.P., A.P.; *Experimentation,* J.R.H., W-Z.Z., S-H.W, E. L. E., S. M., H. A., M. L., M.M.P.; *Live-cell image analysis and interpretation,* J.R.H., M.M.P.; *Formal data analysis,* J.R.H., E. L. E., M.M.P., W-Z.Z., S-H.W, H.A., S.M.; *Visualization,* J.R.H., E.L.E, M.M.P; *Writing – original draft,* J.R.H, M.M.P, E.L.E.; *Writing – review and editing,* M.M.P, E.L.E., J.R.H, A.P., S-H.W., H.A.; all authors read and approved the final draft. *Supervision,* M.M.P and A.P.; *Funding acquisition,* M.M.P and A.P.

Competing Interests

The authors declare no competing interests.

bioRxiv preprint doi: https://doi.org/10.1101/2020.10.18.344598; this version posted October 19, 2020. The copyright holder for this preprint (which was not certified by peer review) is the author/funder, who has granted bioRxiv a license to display the preprint in perpetuity. It is made available under aCC-BY-NC-ND 4.0 International license.

References

1. Kirfel, G. & Herzog, V. Migration of epidermal keratinocytes: mechanisms, regulation, and biological significance. *Protoplasma* **223**, 67–78 (2004).
2. Gantwerker, E. A. & Hom, D. B. Skin: histology and physiology of wound healing. *Facial Plast. Surg. Clin. North Am.* **19**, 441–453 (2011).
3. Mayor, R. & Etienne-Manneville, S. The front and rear of collective cell migration. *Nat. Rev. Mol. Cell Biol.* **17**, 97–109 (2016).
4. Ladoux, B. & Mège, R.-M. Mechanobiology of collective cell behaviours. *Nat. Rev. Mol. Cell Biol.* **18**, 743–757 (2017).
5. Evans, N. D., Oreffo, R. O. C., Healy, E., Thurner, P. J. & Man, Y. H. Epithelial mechanobiology, skin wound healing, and the stem cell niche. *J. Mech. Behav. Biomed. Mater.* **28**, 397–409 (2013).
6. Huang, C., Du, Y. & Ogawa, R. Mechanobiology and Mechanotherapy for Cutaneous Wound-Healing. in *Mechanobiology* (ed. Rawlinson, S. C. F.) vol. 60 239–253 (John Wiley & Sons, Inc., 2017).
7. Rosińczuk, J., Taradaj, J., Dymarek, R. & Sopel, M. Mechanoregulation of Wound Healing and Skin Homeostasis. *Biomed Res. Int.* **2016**, (2016).
8. Brugués, A. *et al.* Forces driving epithelial wound healing. *Nat. Phys.* **10**, 683–690 (2014-9).
9. Hiroyasu, S., Colburn, Z. T. & Jones, J. C. R. A hemidesmosomal protein regulates actin dynamics and traction forces in motile keratinocytes. *FASEB J.* **30**, 2298–2310 (2016-6).
10. Nourse, J. L. & Pathak, M. M. How cells channel their stress: Interplay between Piezo1 and the cytoskeleton. *Semin. Cell Dev. Biol.* (2017) doi:10.1016/j.semcdb.2017.06.018.
11. Murthy, S. E., Dubin, A. E. & Patapoutian, A. Piezos thrive under pressure: mechanically activated ion channels in health and disease. *Nat. Rev. Mol. Cell Biol.* **18**, 771–783 (2017).
12. Li, J. *et al.* Piezo1 integration of vascular architecture with physiological force. *Nature* **515**, 279–282 (2014).
13. Ranade, S. S. *et al.* Piezo1, a mechanically activated ion channel, is required for vascular development in mice. *Proc. Natl. Acad. Sci. U. S. A.* **111**, 10347–10352 (2014).
14. Pathak, M. M. *et al.* Stretch-activated ion channel Piezo1 directs lineage choice in human neural stem cells. *Proc. Natl. Acad. Sci. U. S. A.* **111**, 16148–16153 (2014).
15. Rocio Servin-Vences, M., Moroni, M., Lewin, G. R. & Poole, K. Direct measurement of TRPV4 and PIEZO1 activity reveals multiple mechanotransduction pathways in chondrocytes. *Elife* **6**, e21074 (2017).
16. Zeng, W.-Z. *et al.* PIEZOs mediate neuronal sensing of blood pressure and the baroreceptor reflex. *Science* **362**, 464–467 (2018).
17. Nonomura, K. *et al.* Mechanically activated ion channel PIEZO1 is required for lymphatic valve formation. *Proc. Natl. Acad. Sci. U. S. A.* **115**, 12817–12822 (2018).
18. Cahalan, S. M. *et al.* Piezo1 links mechanical forces to red blood cell volume. *Elife* **4**, (2015).
19. Lee, W. *et al.* Synergy between Piezo1 and Piezo2 channels confers high-strain mechanosensitivity to articular cartilage. *Proc. Natl. Acad. Sci. U. S. A.* **111**, E5114–22 (2014).
20. Gudipaty, S. A. *et al.* Mechanical stretch triggers rapid epithelial cell division through Piezo1. *Nature* **543**, 118–121 (03 02, 2017).
21. Eisenhoffer, G. T. *et al.* Crowding induces live cell extrusion to maintain homeostatic cell numbers in epithelia. *Nature* **484**, 546–549 (2012).

bioRxiv preprint doi: https://doi.org/10.1101/2020.10.18.344598; this version posted October 19, 2020. The copyright holder for this preprint (which was not certified by peer review) is the author/funder, who has granted bioRxiv a license to display the preprint in perpetuity. It is made available under aCC-BY-NC-ND 4.0 International license.

22. Ellefsen, K. L. *et al.* Myosin-II mediated traction forces evoke localized Piezo1-dependent Ca 2+ flickers. *Commun Biol* **2**, 1–13 (2019).
23. Aguilar-Cuenca, R., Juanes-García, A. & Vicente-Manzanares, M. Myosin II in mechanotransduction: master and commander of cell migration, morphogenesis, and cancer. *Cell. Mol. Life Sci.* **71**, 479–492 (2014).
24. Vicente-Manzanares, M., Ma, X., Adelstein, R. S. & Horwitz, A. R. Non-muscle myosin II takes centre stage in cell adhesion and migration. *Nat. Rev. Mol. Cell Biol.* **10**, 778–790 (2009).
25. Coste, B. *et al.* Piezo1 and Piezo2 Are Essential Components of Distinct Mechanically Activated Cation Channels. *Science* **330**, 55–60 (2010).
26. Moehring, F., Mikesell, A. R., Sadler, K. E., Menzel, A. D. & Stucky, C. L. Piezo1 Mediates Keratinocyte Mechanotransduction. *bioRxiv* 2020.07.19.211086 (2020) doi:10.1101/2020.07.19.211086.
27. Ma, S. *et al.* Common PIEZO1 Allele in African Populations Causes RBC Dehydration and Attenuates Plasmodium Infection. *Cell* **173**, 443–455.e12 (2018).
28. Boudaka, A., Saito, C. T. & Tominaga, M. Deletion of TRPV4 enhances in vitro wound healing of murine esophageal keratinocytes. *Sci. Rep.* **10**, 11349 (2020).
29. Takada, H., Furuya, K. & Sokabe, M. Mechanosensitive ATP release from hemichannels and Ca^{2+} influx through TRPC6 accelerate wound closure in keratinocytes. *J. Cell Sci.* **127**, 4159–4171 (2014).
30. Graham, D. M., Huang, L., Robinson, K. R. & Messerli, M. A. Epidermal keratinocyte polarity and motility require Ca^{2+} influx through TRPV1. *J. Cell Sci.* **126**, 4602–4613 (2013).
31. van Helvert, S., Storm, C. & Friedl, P. Mechanoreciprocity in cell migration. *Nat. Cell Biol.* **20**, 8–20 (2018).
32. Gorelik, R. & Gautreau, A. Quantitative and unbiased analysis of directional persistence in cell migration. *Nat. Protoc.* **9**, 1931–1943 (2014).
33. Ridley, A. J. Life at the Leading Edge. *Cell* **145**, 1012–1022 (2011).
34. Petrie, R. J., Doyle, A. D. & Yamada, K. M. Random versus directionally persistent cell migration. *Nat. Rev. Mol. Cell Biol.* **10**, 538–549 (2009).
35. Yam, P. T. *et al.* Actin-myosin network reorganization breaks symmetry at the cell rear to spontaneously initiate polarized cell motility. *J. Cell Biol.* **178**, 1207–1221 (2007).
36. Somlyo, A. P. & Somlyo, A. V. Ca2+ sensitivity of smooth muscle and nonmuscle myosin II: modulated by G proteins, kinases, and myosin phosphatase. *Physiol. Rev.* **83**, 1325–1358 (2003).
37. Ryan, G. L. *et al.* Cell protrusion and retraction driven by fluctuations in actin polymerization: A two-dimensional model. *Cytoskeleton* **74**, 490–503 (2017).
38. Giannone, G. *et al.* Lamellipodial actin mechanically links myosin activity with adhesion-site formation. *Cell* **128**, 561–575 (2007).
39. Giannone, G. *et al.* Periodic lamellipodial contractions correlate with rearward actin waves. *Cell* **116**, 431–443 (2004).
40. Jakobs, M. A., Dimitracopoulos, A. & Franze, K. KymoButler, a deep learning software for automated kymograph analysis. *Elife* **8**, (2019).
41. Wei, C., Wang, X., Zheng, M. & Cheng, H. Calcium gradients underlying cell migration. *Curr. Opin. Cell Biol.* **24**, 254–261 (2012).

bioRxiv preprint doi: https://doi.org/10.1101/2020.10.18.344598; this version posted October 19, 2020. The copyright holder for this preprint (which was not certified by peer review) is the author/funder, who has granted bioRxiv a license to display the preprint in perpetuity. It is made available under aCC-BY-NC-ND 4.0 International license.

42. Tsai, F.-C., Kuo, G.-H., Chang, S.-W. & Tsai, P.-J. Ca2+ signaling in cytoskeletal reorganization, cell migration, and cancer metastasis. *Biomed Res. Int.* **2015**, 409245 (2015).
43. Canales, J. *et al.* A TR(i)P to cell migration: New roles of TRP channels in mechanotransduction and cancer. *Front. Physiol.* **10**, 757 (2019).
44. Lee, J., Ishihara, A., Oxford, G., Johnson, B. & Jacobson, K. Regulation of cell movement is mediated by stretch-activated calcium channels. *Nature* **400**, 382–386 (1999).
45. Doyle, A., Marganski, W. & Lee, J. Calcium transients induce spatially coordinated increases in traction force during the movement of fish keratocytes. *J. Cell Sci.* **117**, 2203–2214 (2004).
46. Wei, C. *et al.* Calcium flickers steer cell migration. *Nature* **457**, 901–905 (2009).
47. Tsai, F.-C. & Meyer, T. Ca2+ pulses control local cycles of lamellipodia retraction and adhesion along the front of migrating cells. *Curr. Biol.* **22**, 837–842 (2012).
48. Patkunarajah, A. *et al.* TMEM87a/Elkin1, a component of a novel mechanoelectrical transduction pathway, modulates melanoma adhesion and migration. *Elife* **9**, (2020).
49. Maneshi, M. M., Ziegler, L., Sachs, F., Hua, S. Z. & Gottlieb, P. A. Enantiomeric Aβ peptides inhibit the fluid shear stress response of PIEZO1. *Sci. Rep.* **8**, 14267 (2018).
50. McHugh, B. J., Murdoch, A., Haslett, C. & Sethi, T. Loss of the Integrin-Activating Transmembrane Protein Fam38A (Piezo1) Promotes a Switch to a Reduced Integrin-Dependent Mode of Cell Migration. *PLoS One* **7**, e40346 (2012).
51. Chubinskiy-Nadezhdin, V. I. *et al.* Agonist-induced Piezo1 activation suppresses migration of transformed fibroblasts. *Biochem. Biophys. Res. Commun.* **514**, 173–179 (2019).
52. Hung, W.-C. *et al.* Confinement Sensing and Signal Optimization via Piezo1/PKA and Myosin II Pathways. *Cell Rep.* **15**, 1430–1441 (2016).
53. Li, C. *et al.* Piezo1 forms mechanosensitive ion channels in the human MCF-7 breast cancer cell line. *Sci. Rep.* **5**, 8364 (2015).
54. Cramer, L. P. Mechanism of cell rear retraction in migrating cells. *Curr. Opin. Cell Biol.* **25**, 591–599 (2013).
55. Piccinini, F., Kiss, A. & Horvath, P. CellTracker (not only) for dummies. *Bioinformatics* **32**, 955–957 (2016).
56. Berg, S. *et al.* ilastik: interactive machine learning for (bio)image analysis. *Nat. Methods* **16**, 1226–1232 (2019).

bioRxiv preprint doi: https://doi.org/10.1101/2020.10.18.344598; this version posted October 19, 2020. The copyright holder for this preprint (which was not certified by peer review) is the author/funder, who has granted bioRxiv a license to display the preprint in perpetuity. It is made available under aCC-BY-NC-ND 4.0 International license.

Methods

Animals

All studies were approved by the Institutional Animal Care and Use Committee of University of California at Irvine and The Scripps Research Institute, as appropriate, and performed in accordance with their guidelines. *Piezo1* LacZ reporter mice (JAX stock 026948) and *Piezo1*-tdTomato reporter mice, expressing a C-terminal fusion of *Piezo1* with tdTomato (*Piezo1*-tdTomato; JAX stock 029214), were generated in a previous study [13]. Skin specific *Piezo1*-cKO mice were generated by breeding *Piezo1*$^{fl/fl}$ *mice* [18] (Jax stock 029213) with K14-Cre (The Jackson Laboratory, stock 004782). Skin specific *Piezo1*-GoF mice were generated by breeding *Piezo1*$^{cx/cx}$ mice [27] with K14-Cre.

Keratinocyte isolation

P0-P1 mice were anesthetized with ice prior to decapitation. Bodies were placed in 10% povidone for 1 minute, rinsed with sterile PBS, prior to soaking in 70% ethanol for a further minute, and rinsed again with sterile PBS. Subsequently, the entire dorsal skin was separated from the body. Dorsal skin was left to dissociate in either 0.25% Trypsin/EDTA (Gibco) for 1 hour or 1x dispase solution (Cellntec CnT-DNP-10) at 4°C overnight for 15-18 hours. After incubation, the epidermis was gently separated from the dermis, laid flat, dorsal side down in Accutase (CellnTec CnT-Accutase-100) and incubated for 30 minutes at room temperature. The epidermis was then transferred to a dish of either CnT-02 or CnT-Pr media (CellnTec), supplemented with 10% FBS and 1% Penicillin/Streptomycin. The epidermis was cut into small pieces with scissors prior to agitation on a stir plate for 30 minutes. Cells were then filtered through a 70 µm cell strainer (Falcon) and spun down at 1200 rpm for 5 minutes. The pellet was resuspended in CnT-Pr media (CellnTec) supplemented with ISO-50 (1:1000) (CellnTec) and Gentamicin (50 µg/mL) (ThermoFisher), prior to counting and plating.

Keratinocyte Culture

For live cell imaging, primary keratinocytes were plated on #1.5 glass-bottom dishes (Mat-Tek Corporation) coated with 10µg/ml fibronectin (Fisher Scientific, CB-40008A). For monolayer experiments cells were plated at $1.5x10^5$ cells/dish in the 14-mm glass region of dishes. For sparse cell migration experiments and for Ca^{2+} imaging experiments cells were plated at $1.5x10^4$ cells/dish in the 14-mm glass region of dishes. Keratinocytes were imaged following at least 2 days in Cnt-Pr-D (CellnTec) differentiation media.

Real-time quantitative PCR

After initial keratinocyte isolation and filtering through a 70 µm cell strainer, cells were filtered again through a 40 µm strainer. The filtered solution was spun down and a cell pellet was obtained for RNA isolation. Total RNA was isolated using the RNeasy kit (Qiagen), following which cDNA was synthesized using Superscript III (Invitrogen) and was used for subsequent qPCR experiments (ABI 7900HT fast real time system). qPCR probes (Thermofisher) used were *Piezo1*: Assay ID Mm01241570_g1; ACTGAGAGGATGTTCAGCCAGAATG and Gapdh: Assay ID Mm99999915_g1.

X-Gal/LacZ staining

Dorsal skin was harvested as described above, cryopreserved in OCT and sectioned into

bioRxiv preprint doi: https://doi.org/10.1101/2020.10.18.344598; this version posted October 19, 2020. The copyright holder for this preprint (which was not certified by peer review) is the author/funder, who has granted bioRxiv a license to display the preprint in perpetuity. It is made available under aCC-BY-NC-ND 4.0 International license.

8 µm thick slices. Skin cryosections were allowed to completely dry prior to being fixed in "fix buffer" composed of 1X PBS, 5 mM EGTA (Sigma cat. # E4378), 2 mM $MgCl_2$, 0.2% glutaraldehyde (Sigma cat. # G-7776), pH 7.4 for 15 minutes at room temperature. Next they were washed with "wash buffer" composed of 1X PBS, 2 mM $MgCl_2$ twice for 5 minutes each. X-gal staining buffer composed of 1X PBS, 2 mM $MgCl_2$, 5 mM potassium ferrocyanide [$K_4Fe(CN)_6 \cdot 3H_20$] (Sigma cat. # P-9287), 5 mM potassium ferricyanide [$K_3Fe(CN)_6$] (Sigma cat. #P-8131), and 1 mg/ml X-gal [5-bromo-4-chloro-3-indolyl-β-D-galactoside] was made fresh. Then, tissue slides were incubated overnight at 37°C in the "X-gal staining buffer" inside a humidified chamber. The following day, slides were rinsed with 1X PBS and counterstained with Nuclear Fast Red. Slides were then fixed with 4% PFA for longer preservation.

Immunofluorescence staining

Immunostaining of fixed keratinocytes in Figure 3A was performed as previously described [14,22] using primary antibody Goat anti-RFP (Rockland, Cat#200-101-379), 1:200 (5 µg/ml). Secondary antibody used was Donkey anti-goat Alexa Fluor 555 (Invitrogen, Cat#A21432), 1:500. Nuclei were stained by Hoechst (ThermoFisher, Cat#H1399) at 6 µg/ml in PBS. Samples were labeled in Mat-Tek dishes.

For immunostaining of skin sections in Supplementary Figure 3, dorsal skin was prepared and sectioned as for X-Gal staining. Skin cryosections were fixed for 10 minutes in cold acetone, washed twice in 1X PBS prior to blocking for 30 minutes in 10% normal goat serum at room temperature. Primary antibodies used were Rabbit anti-Keratin 14 (Covance, Cat# PRB-155P), 1:1000 (1 µg/ml) and Rabbit anti-Keratin 10 (Covance, Cat# PRB-159P), 1:1000 (1 µg/ml). Secondary antibody used was Goat anti-Rabbit Alexa Fluor 488 (Invitrogen, Cat#A11008), 1:1000. Nuclei were stained by DAPI (Invitrogen, Cat#D1306), 1:50,000. All antibody incubations were performed at room temperature, for 1 hour in 1% BSA in PBS. Slides were mounted in gelvatol containing DAPI.

Microscopy and image analysis

Microscopy

Unless otherwise stated, *in vitro* images were taken using an Olympus IX83-ZDC microscope, equipped with an automated 4-line cellTIRF illuminator. A full enclosure environmental chamber (Tokai Hit) allowed cells to be imaged at 37°C with 5% CO_2 ensuring optimal cell health during time-lapse experiments. Stage movement was controlled by a programmable motorized stage (ASI) while an Olympus ZDC autofocus control unit allowed for samples to remain in focus throughout imaging periods. The open-source microscopy software µManager was used to control the microscope and acquire images for all except Figure 1A, 4E and Supp Fig 2, 3. Images for Figure 1C, 1E, 2B, 2E, 3, and Supplementary Videos 1, 2, 4, 6, 7, 8, 9, 10 were taken using a PLAPO 60x oil immersion objective with a numerical aperture of 1.45. Images for Figure 3A were taken using a PLAPO 60x oil immersion objective with a numerical aperture of 1.50. Images for Figure 2C, 2D and Supplementary Video 5 were taken using a UPlanSApo 40x dry objective with a numerical aperture of 0.95. Images for Figure 4A, 4B and Supplementary Videos 3, 11 were taken using a UPlanSApo 10x dry objective with a numerical aperture of 0.40. Images for Figure 1C, 1E, 2B, 2C, 2D, 2E, 3A, 3B, 3C, 3D, 3E, 3F, 4A, 4B, and all Supplementary Videos were acquired using a Hamamatsu Flash 4.0 v2+ scientific CMOS camera. Images for

bioRxiv preprint doi: https://doi.org/10.1101/2020.10.18.344598; this version posted October 19, 2020. The copyright holder for this preprint (which was not certified by peer review) is the author/funder, who has granted bioRxiv a license to display the preprint in perpetuity. It is made available under aCC-BY-NC-ND 4.0 International license.

Figure 2A were acquired using a Hamamatsu Fusion camera. Images for Supplementary Figure 1B were taken using a Hamamatsu C4742-95-12ER Digital CCD camera.

Imaging Piezo1 Ca^{2+} flickers (Fig.1 C-F; Supplementary Videos 1-2)

As described previously, [22] TIRF microscopy was used for the detection of Ca^{2+} flickers. Keratinocytes were loaded through the incubation of 2 µM Cal-520 AM (AAT Bioquest Inc.) with 0.04% Pluronic F-127 (ThermoFisher) in phenol red-free DMEM-F12 (Cat#11039047, Gibco) for 30-35 minutes at 37°C, washed three times, and incubated at room temperature for 10–15 minutes prior to imaging. Cells were imaged at room temperature in a bath solution comprising 148 mM NaCl, 3 mM KCl, 3 mM $CaCl_2$, 2 mM $MgCl_2$, 8 mM glucose, and 10 mM HEPES (pH adjusted to 7.3 with NaOH, Osmolarity adjusted to 313 mOsm/kg with sucrose). Cal-520 fluorescence was elicited by excitation with a 488 nm laser line and images were acquired at a frame rate of 9.54 frames/second.

Piezo1 Ca^{2+} flicker analysis (Fig.1 C-F; Supplementary Videos 1-2)

Ca^{2+} flickers were automatically detected as previously described [22] using the detect_puffs plugin (https://github.com/kyleellefsen/detect_puffs) for the open-source image processing program, Flika (https://flika-org.github.io/#). This plugin was used to identify and localize flicker events in recorded videos. Each video is a microscope field of view which contains one or more keratinocytes. To normalize any potential variability in cell number or size between samples, flicker frequency by cell area was computed for each field of view. Cell area was measured by using the ImageJ plugin SIOX: Simple Interactive Object Extraction to create binary masks and compute cell area.

Single Cell Tracking Assay (Fig.1 G-J; Supp. Fig. 3)

Primary keratinocytes sparsely seeded on fibronectin-coated glass-bottom dishes were allowed to migrate freely for up to 16.67 hours at 37°C with 5% CO_2 in bath solution composed of Cnt-Pr-D (CellnTec) culture media with extracellular Ca^{2+} concentration adjusted to 1.2 mM. Timelapse DIC images at multiple microscope fields of view were acquired in each dish of cells at 5 minute intervals for the imaging period. When collecting trajectories we only considered cells which (1) stay within the field of view during the imaging period and (2) did not come into contact with other keratinocytes. The center of the cell body was the tracked position of the cell. The initial positions of cells were manually identified, after which the positions of migrating cells were automatically tracked using the Cell Tracker software (http://www.celltracker.website/index.html) [55]. Cell trajectories were logged and exported into Microsoft Excel. Further analysis was subsequently performed using the published open-source algorithm, DiPer [32] to obtain average instantaneous speed, mean squared displacement (MSD), directionality analysis and trajectory flower plots.

Migration dynamics assay (Fig. 2C-E; Supplementary Videos 5-7)

Cells were imaged via DIC microscopy at 37°C with 5% CO_2, with snapshots taken at 5 second intervals for at least 30 minutes in Cnt-Pr-D culture media (CellnTec) with added 1.2 mM Ca^{2+} and 0.0004% DMSO. After acquiring baseline images, the media was changed and 4 µM Yoda1 was added to the bath solution. After allowing the drug to act for 5-7 minutes, imaging was resumed for at least 55 minutes. Experiments were performed multiple times on indepen-

bioRxiv preprint doi: https://doi.org/10.1101/2020.10.18.344598; this version posted October 19, 2020. The copyright holder for this preprint (which was not certified by peer review) is the author/funder, who has granted bioRxiv a license to display the preprint in perpetuity. It is made available under aCC-BY-NC-ND 4.0 International license.

dent experiment days. Kymographs were created from representative cells using the ImageJ plugin KymoResliceWide (https://imagej.net/KymoResliceWide). Kymographs were built by taking 1 pixel width lines at regions of interest (ROI) along the cell's leading edge (Fig. 2).

PIEZO1-tdTomato time-lapse imaging (Fig. 2B,3, Supplementary Videos 4, 8-10)

Primary PIEZO1-tdTomato keratinocytes were cultured either sparsely or as confluent monolayers. Monolayers were scratched using a 10 µL pipette tip immediately prior to imaging. Experiments were performed in Cnt-Pr-D (CellnTec) culture media with added 1.2 mM Ca^{2+}. Either single cells or, for monolayer scratch experiments, regions along the initial wound edge were marked using a programmable stage and imaged throughout the imaging period as cells migrated to close the wound. PIEZO1-tdTomato channels were illuminated using a 561 nm laser and imaged using TIRF microscopy. TIRF and DIC snapshots at regions of interest were sequentially acquired every 10 (Figures 3 C, D, E, F Supplementary Video 9, 10) or 30 (Figures 3 A, B, Supplementary Figure 5, Supplementary Video 8) minutes over the course of up to 16.67 hours. Time-lapse images were processed from the original recording by subtracting every frame of a movie by (1) the median value z-projection image and then (2) the minimum value z-projection image. KymoResliceWide was then used to construct kymographs by taking the average intensity of the transverse of a 100 pixel wide line drawn at ROIs along the wound edge. ROIs were chosen so that they would capture the wound edge for the entire duration it was present within the microscope field of view. At least one kymograph was generated from each unique microscope field of view. Impartial identification and tracking of periods of channel enrichment was performed using the Kymobutler tool in Wolfram Mathematica (https://gitlab.com/deep-mirror/kymobutler). Only puncta located at the wound edge that were successfully tracked for at least 70 minutes were collected for further analyses. The pixel classification function of the computer vision software, Ilastik (https://www.ilastik.org/) [56] was used to classify DIC images and create binarized movies used for generating binarized kymographs in Figure 3 E,F.

Wound edge dynamics assay (Fig. 4A, 4B, Supplementary Video 11)

Primary keratinocytes were densely seeded and cultured to form monolayers. Scratch wounds were generated by scratching monolayers with a 10 µl pipette tip immediately prior to imaging. Dishes were washed 3x with cell culture media to remove cell debris. Yoda1 (4 µM) or equivalent concentration of DMSO control was added to the bath media immediately prior to imaging. DIC snapshots were taken every 5 minutes at ROIs along the wound edge for at least 9 hours. Representative kymographs were created using 1 pixel wide ROIs using KymoResliceWide. Binarized movies generated by using the ImageJ plugin Trainable Weka Segmentation (https://imagej.net/Trainable_Weka_Segmentation) were used to create binarized kymographs.

In vitro wound healing assay (Fig. 4C-D)

Primary keratinocytes were seeded in a two-well silicone insert in a 35 mm dish (ibidi, 81176). Cells were cultured until a monolayer confluence was reached. Subsequently, the insert was removed from the dish to create a reproducible 500 µm cell-free gap. The dishes were washed with cell culture medium to remove floating cells and cell debris. For pharmacology experiments, Yoda1 (4 µM) or equivalent concentration of DMSO control was added into the dishes immediately prior to imaging. Dishes were imaged by phase-contrast microscopy at 37°C

bioRxiv preprint doi: https://doi.org/10.1101/2020.10.18.344598; this version posted October 19, 2020. The copyright holder for this preprint (which was not certified by peer review) is the author/funder, who has granted bioRxiv a license to display the preprint in perpetuity. It is made available under aCC-BY-NC-ND 4.0 International license.

(5% CO_2) for indicated time points.

In vivo wound healing assay

Adult (3-4 month) male and female mice were anaesthetized with isoflurane and placed on a heated blanket. The dorsal hair was shaved and further removed by hair-removal cream. Two full-thickness wounds were created in the upper dorsal skin using a 4 mm wide dermal biopsy punch (Integra LifeSciences Corporation). Wounded areas were patched with medical dressing, Tegaderm (3M). Wound sizes were measured with a scale loupe (Peak Optics, #1975) at Day 6 to compare healing progress. Both the short (dS) and long (dL) diameters of the oval-shaped wounds were measured and used to calculate an overall wound area using the equation: dS x dL x π.

Statistical Analysis

All of the data are presented as the mean ± SEM. Sample sizes are indicated in corresponding figure legends. OriginPro 2020 (OriginLab Corporation) was used for statistical analysis and generating plots. *P* values and statistical tests used are indicated in figure legends. Unless otherwise stated, a two-sample *t*-test was used where data were modeled by a normal distribution and the nonparametric Kolmogorov–Smirnov test was used in the case of non-normal distributions.